# Biasing of Capacitive Micromachined Ultrasonic Transducers

Giosuè Caliano, *Senior Member, IEEE*, Giulia Matrone, *Member, IEEE*, and Alessandro Stuart Savoia, *Member, IEEE*

***Abstract*— Capacitive micromachined ultrasonic transducers (CMUTs) represent an effective alternative to piezoelectric transducers for medical ultrasound imaging applications. They are microelectromechanical devices fabricated using silicon micromachining techniques, developed in the last two decades in many laboratories. The interest for this novel transducer technology relies on its full compatibility with standard integrated circuit technology that makes it possible to integrate on the same chip the transducers and the electronics, thus enabling the realization of extremely low-cost and high-performance devices, including both 1-D or 2-D arrays. Being capacitive transducers, CMUTs require a high bias voltage to be properly operated in pulse-echo imaging applications. The typical bias supply residual ripple of high-quality high-voltage (HV) generators is in the millivolt range, which is comparable with the amplitude of the received echo signals, and it is particularly difficult to minimize. The aim of this paper is to analyze the classical CMUT biasing circuits, highlighting the features of each one, and to propose two novel HV generator architectures optimized for CMUT biasing applications. The first circuit proposed is an ultralow-residual ripple (<5 $\mu$V) HV generator that uses an extremely stable sinusoidal power oscillator topology. The second circuit employs a commercially available integrated step-up converter characterized by a particularly efficient switching topology. The circuit is used to bias the CMUT by charging a buffer capacitor synchronously with the pulsing sequence, thus reducing the impact of the switching noise on the received echo signals. The small area of the circuit (about 1.5 cm$^2$) makes it possible to generate the bias voltage inside the probe, very close to the CMUT, making the proposed solution attractive for portable applications. Measurements and experiments are shown to demonstrate the effectiveness of the new approaches presented.**

***Index Terms*— Bias voltage, capacitive micromachined ultrasonic transducers (CMUTs), capacitive transducer, high-voltage (HV) generator, ripple rejection, synchronous biasing.**

## I. Introduction

THE availability of ultrasonic transducers with suitable performance is crucial for the development of any high-resolution pulse-echo ultrasound imaging system. The characteristics of the transducer determine the final image quality. A large bandwidth is important, since the pulse length determines the axial resolution of the system, while the transducer aperture and wavelength define its lateral resolution. Any type of noise added to the echo signals collected by the probe (normally characterized by a very large dynamic range, up to 80–100 dB) and processed by the scanner results in a degradation of the reconstructed image quality.

In recent years, the major semiconductor manufacturers have developed a wide range of analog components such as low-noise amplifiers (LNAs) and variable-gain amplifiers (VGAs) for ultrasound imaging applications. The bandwidths of these components are about 50–120 MHz[1] and the dynamic ranges are about 85–97 dB, which are well matched with most commercial ultrasound transducers [1]. As the high-frequency acoustic signals penetrate through the body, they are attenuated by about 1 dB/cm/MHz. For example, with an 8-MHz probe and 4-cm depth penetration, accounting for the two-way propagation path, the amplitude of the echo signals coming from the deeper tissues will differ by 64 dB from those generated by superficial tissues. Adding 50 dB of image dynamic range, and accounting for losses due to bone, cables, and other mismatches, the required dynamic range approaches 120 dB. This establishes a practical limit for the dynamic range between 100 and 120 dB.

To give an idea of the amplitude range of the signals that can be detected by an ultrasound imaging system front-end circuit, we bring the example of an LNA with a maximum input signal amplitude of 500 $\mathrm{mV_{pk-pk}}$ and a dynamic range of 97 dB, resulting in a minimum signal amplitude of about 7 $\mu\mathrm{V_{pk-pk}}$.

Capacitive micromachined ultrasonic transducers (CMUTs) represent today the most promising devices for the next generation of ultrasound imaging probes [2]. These are microelectromechanical devices fabricated using silicon micromachining techniques [3]–[7] developed in the last two decades in many laboratories, and also by some of the authors of this paper. In the past decade, their use has proved to be attractive, mainly in the field of medical ultrasound imaging [6], [7]. The growing interest for this new technology is based on its full compatibility with the standard integrated circuit (IC) technology that allows integrating, on the same chip, the transducers and the electronics, thereby enabling the realization of low-cost devices with high performance [9]–[14]. From a practical point of view, CMUTs have been widely recognized as a valuable alternative to piezoelectric transducer technology in a variety of medical imaging and biometric applications, thanks

Manuscript received July 21, 2016; accepted October 27, 2016. Date of publication October 28, 2016; date of current version February 1, 2017. This work was supported in part by the Italian Ministry of Education, University and Research (MIUR) within the framework of the PRIN 2010-2011.

G. Caliano and A. S. Savoia are with the Dipartimento di Ingegneria, Università degli Studi Roma Tre, 00146 Rome, Italy (e-mail: giosue.caliano@uniroma3.it).

G. Matrone is with the Dipartimento di Ingegneria Industriale e dell'Informazione, Università degli Studi di Pavia, 27100 Pavia, Italy.

Digital Object Identifier 10.1109/TUFFC.2016.2623221

[1]The AD8331 (Analog Devices, Norwood, MA, USA) ultralow-noise VGA has a preamplifier with a −3 dB bandwidth of 120 MHz.

to the higher sensitivity, wider bandwidth, and improved thermal efficiency [15]–[18]. On the other hand, this technology has suffered from some initial technical limitations, gradually overcome by research efforts, and also the high development costs have made the introduction of these new devices still very slow. However, thanks to the latest research advances and the growing interest among the semiconductor manufacturers, these devices are becoming more attractive for large medical devices companies.

Being capacitive transducers, CMUTs require a bias voltage to be both linearly operated in transmission and to provide electrical signal generation capability in reception [2]. Moreover, CMUT biasing is strictly required in those applications where linearity is desirable, such as ultrasound imaging [6]. Depending on the CMUT design and fabrication technology, the bias voltage needed to operate efficiently may be relatively high ($>100$ V). In this case, the residual ripple noise that typically affects high-voltage (HV) generators used for CMUT biasing is detected by the readout circuits as a valid signal, and it is particularly difficult to minimize. In fact, currently available high-quality and HV laboratory power supplies are capable of generating hundreds of volts with a residual ripple, at best, in the millivolt range.[2] In ultrasound medical imaging applications, such noise level may be of the same order of magnitude of the echo signals. Furthermore, for efficiency reasons, switching circuits are often used in HV power supply units of ultrasound imaging systems, whereby it is necessary that the switching frequencies and their harmonics fall outside the system bandwidth. Normally, switching regulator configurations cannot achieve a low-noise performance level. Even though sophisticated circuital solutions may be adopted, it is challenging to efficiently generate high dc voltages over 100 V keeping the ripple noise below 100 $\mu V_{pk-pk}$ inside the frequency band of interest [8].

In general, considering the typical voltage values for medical imaging CMUTs [19], a biasing circuit must be capable of generating a maximum voltage of about 300 V dc with a residual ripple amplitude lower than 5–10 $\mu V_{pk-pk}$ in the frequency band of the ultrasound imaging system receiver (i.e., 1–20 MHz), in order to be considered as an efficient bias generator, with negligible effect on the image quality.

In this paper, we first introduce some simple models used to analyze the receiving CMUT operation in relation to the applied bias voltage. Then, we describe the typical biasing network circuits used to couple a bias voltage to a CMUT array, partly already presented in [20]–[25], and we analyze their performance in terms of biasing noise rejection. We then propose two novel high-bias-voltage generator circuits, based on different approaches and designed to be used in different contexts. The first biasing circuit proposed implements a particular technique to achieve the high dc voltage required for CMUT biasing with an extremely low residual ripple. Such a circuit uses a sinusoidal oscillator to obtain a "step-up" characteristic, i.e., a dc-to-dc power converter with an output voltage greater than its input voltage. Since the power consumption of the circuit is quite high (14 W), and the physical dimensions of the realized prototype (100 $cm^2$) are constrained by the size of the components, the proposed circuit has to be integrated in the scanner system chassis, and the biasing signal must be routed to the probe using a suitable cable, in addition to those used to connect the pulse-echo signals from the system to the probe and vice versa. Therefore, such an approach is suitable for "cart-based" ultrasound scanners. The second biasing circuit proposed uses a different approach to generate the high dc voltage. The basic idea is to use a small and efficient circuit, able to generate HVs thanks to a high output current capability, but characterized by a very high switching noise, synchronized with the scan timing of the ultrasound imaging system, and activated only when the system is not in receiving mode. The circuit is used to charge a buffer capacitor, which maintains the dc bias voltage during the acquisition time while the circuit is turned OFF. This circuit is realized on a very small area (about 1.5 $cm^2$, i.e., 60 times smaller than the previous one), making it possible to integrate it inside the probe, and thus generating the high dc bias voltage very close to the transducer. Such low-power and small-size features make the circuit suitable for portable ultrasound scanners.

The two circuits have been realized and characterized. Both electrical measurements and ultrasound imaging experiments demonstrate the validity of the new approaches here presented.

This paper is organized as follows. In Section II, we describe the main CMUT bias voltage coupling circuits and we analyze their characteristics in terms of noise rejection performance. In Section III, we describe the two proposed CMUT biasing generator architectures. We dedicate Section IV to the characterization of the two generator prototypes, carried out by means of electrical measurements and B-mode ultrasound imaging experiments. Finally, we report the conclusions in Section V.

## II. DC Biasing of CMUT Arrays

A CMUT cell is an electrostatically actuated ultrasonic transducer realized with a flexural plate suspended above a substrate. Each element of a CMUT transducer array, normally used in ultrasound imaging systems, consists of several CMUT cells connected and operating in parallel. The array elements are provided with their own individual electrodes, and they share one common electrode.

A CMUT transducer array can be employed to either transmit or receive ultrasonic acoustic signals. Acoustic wave transmission is accomplished by applying a time-varying voltage signal across the CMUT electrodes, thus making the flexural plates able to vibrate. Reception signal generation occurs when an impinging acoustic wave makes the plates vibrate, inducing the variation of the distance between the upper and lower electrodes, i.e., the "gap," and hence a modulation of the equivalent capacitance [26].

In order to simply illustrate the dependence of the reception signal on the bias voltage, we use the scheme shown in Fig. 1. If linearity is required, a dc charge may be stored in the

[2]As an example, we report the specification of the high-voltage power supply TOE 8842-130 (Toellner Electronic Insrumente GmbH, Herdecke, Germany), which features a maximum dc voltage of 130 V with a residual ripple level of 1 $mV_{rms}$ in the 10 Hz–1 MHz frequency range.

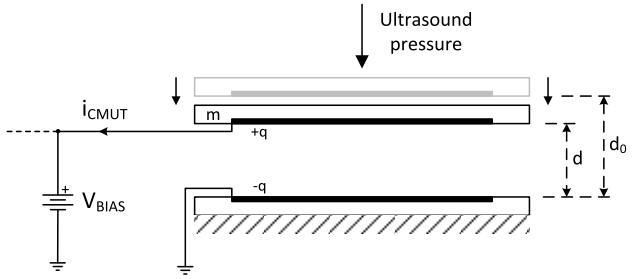


Fig. 1. Simple scheme of a CMUT cell in reception mode: the impinging acoustic wave makes the plate $m$ vibrate, causing a modulation of the gap $d$ and of the equivalent capacitance.

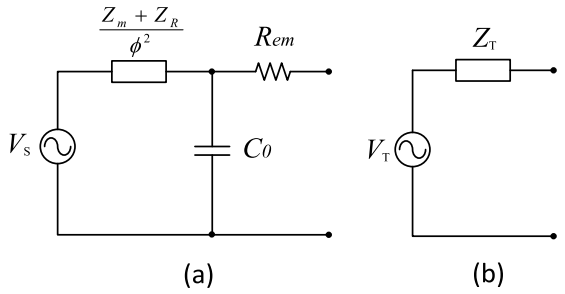


Fig. 2. (a) Equivalent circuit of the CMUT transducer. (b) Its Thévenin reduction.

CMUT during transmit and receive operation by applying a bias voltage. In transmit mode, the electrical signal applied to the CMUT cells consists of a voltage signal added to a constant bias voltage $V_{\mathrm{BIAS}}$. In receive mode, only the bias voltage is applied to the CMUT cells, and the gap between the electrodes changes in response to an impinging acoustic signal, causing the capacitance to vary according to

$$C(t) = \frac{\epsilon_0 \cdot A}{d_0 - d(t)} \tag{1}$$

where $C(t)$ is the capacitance of a single CMUT cell, $\varepsilon_0$ is the vacuum permittivity, $A$ is the area of the electrodes, $d_0$ is the static gap distance, and $d(t)$ is the variation of the gap caused by the impinging ultrasound pressure [14]. The variation of the gap generates a current signal ($i_{\mathrm{CMUT}}$ in Fig. 1) that can be expressed by

$$i_{\mathrm{CMUT}}(t) = \frac{dQ}{dt} = C(t)\frac{dV}{dt} + V(t)\frac{dC}{dt} \tag{2}$$

where $Q(t)$ is the charge stored in the CMUT and $V(t)$ is the voltage across the CMUT electrodes. If the electrical load impedance seen by the CMUT is zero, which is the case of an ideal dc voltage generator, $V(t) = V_{\mathrm{BIAS}}$, so (2), becomes

$$i_{\mathrm{CMUT}} = V_{\mathrm{BIAS}}\frac{dC(t)}{dt} = V_{\mathrm{BIAS}} \cdot \epsilon_0 \cdot A \cdot \frac{d}{dt}\left(\frac{1}{d_0 - d(t)}\right) \tag{3}$$

and finally

$$i_{\mathrm{CMUT}} = V_{\mathrm{BIAS}} \cdot \frac{C(t)^2}{\epsilon_0 . A} \cdot \frac{\partial d(t)}{\partial t} \tag{4}$$

where the term $\partial d(t)/\partial t$ is the velocity of the membrane. Equation (4) shows that the current signal generated by the CMUT cells in reception directly depends on the biasing voltage, so that any signal possibly superimposed to the bias voltage is in turn added to the current signal generated: hence, the need to use a bias voltage, as far as possible, free of residual ripple noise [22]–[25].

In order to properly analyze all the possible biasing circuit configurations and the effect of the residual ripple generated by the bias generators, we introduce the simplified electrical model of the CMUT cell [27] shown in Fig. 2.

Referring to Fig. 2(a), $C_0$ is the shunt capacitance, $R_{em}$ is the series electrical resistance of the plate metallization, and the complex impedance $(Z_m + Z_R)/\phi^2$ represents the total mechanical impedance, including the radiation term, of the CMUT divided by $\phi^2$, which is the electromechanical transformation factor, given by

$$\Phi = \frac{C_0 \cdot V_{\mathrm{BIAS}}}{d_0}. \tag{5}$$

Both $C_0$ and $d_0$, and hence $\phi$, depend on $V_{\mathrm{BIAS}}$. $Z_m$ and $Z_R$ are, respectively, the mechanical and radiation impedances of the CMUT.

By denoting the open-circuit voltage sensitivity of the CMUT as $S_{v0}$, and relating $V_S$ to the incident acoustic pressure $p_S$, the mean squared voltage $\bar{V_S^2}$ is

$$\overline{V_S^2} = |S_{v0}|^2 \cdot \bar{p_s^2}. \tag{6}$$

The equivalent circuit of the CMUT in receive mode can be reduced to the one shown in Fig. 2(b), i.e., its Thévenin reduction, which consists of the equivalent voltage signal $V_T$ and the input electrical impedance of the CMUT, $Z_T$

$$V_T = V_S \cdot \frac{\Phi^2}{\Phi^2 + j\omega C_0(Z_m + Z_R)} \tag{7}$$

$$Z_T = \frac{(Z_m + Z_R)}{\Phi^2 + j\omega C_0 \cdot (Z_m + Z_r)} + R_{em}. \tag{8}$$

In Fig. 3, the two circuits typically used to bias a CMUT array are depicted. In the configuration in Fig. 3(a), that we call *direct biasing,* for each array element $CMUT_i$, the bias voltage is applied through a resistor $R_B$ to the electrode, and the signal is decoupled by a capacitor $C_{Ci}$. In the configuration of Fig. 3(b), called *indirect biasing*, the bias voltage is applied through a resistor $R_B$ to a common electrode, i.e., to the electrode opposite to the signal electrode, and the CMUT itself behaves as a decoupling capacitance. In this case, the common electrode is connected to ground through the $C_C$ capacitor.

In the *direct biasing* case, $n$ resistors and $n$ capacitors are needed. On the other hand, in the *indirect biasing* case, the use of a single resistor and a single capacitor for the entire array is possible. However, the drawback of this last configuration is that, in the event of an electrical failure of a single element such as a short circuit between the CMUT electrodes, a drop of the common electrode potential occurs, caused by a low-resistance path toward ground (i.e., the input stage of a receiver), and the entire array may become unusable. Anyway, the addition of $n$ decoupling capacitors ($C_{Ci}$) to the $n$ output nodes of the array (similar to the *direct biasing* scheme) can overcome this problem. Although presenting the

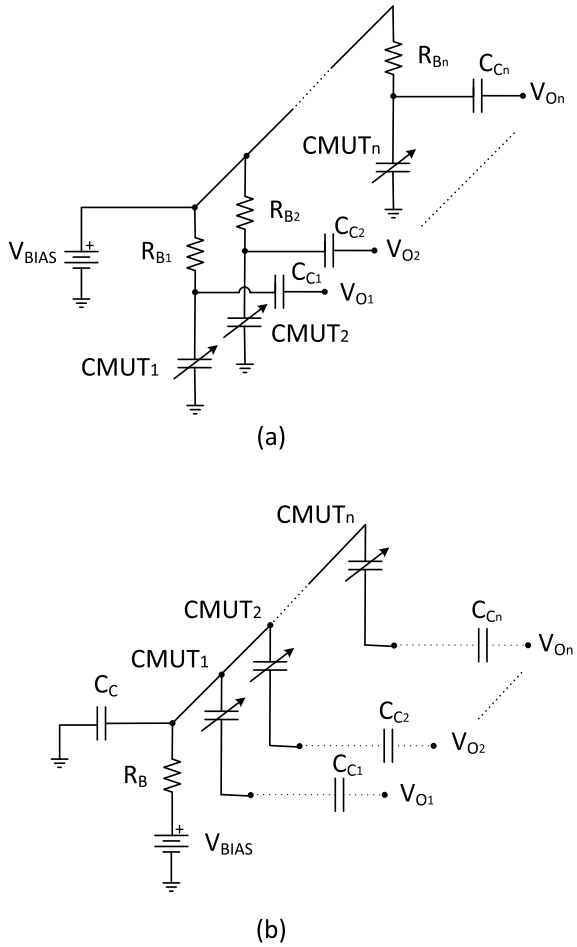


Fig. 3. Two basic schemes for CMUT biasing. (a) Direct biasing. (b) Indirect biasing.

advantage of the lower number of components, in the *direct biasing* configuration, the high dc bias voltage is applied on the common electrode, connected to the ground in ac, which is preferably realized on the front face of the CMUT, for electromagnetic shielding purposes. In the case of failure of the front-face dielectric isolation, this aspect could represent a disadvantage in terms of safety.

In Fig. 4, the basic models for a CMUT using the *direct* [Fig. 4(a)] and *indirect* [Fig. 4(b)] *biasing* configurations are depicted, where $V_n$ is a noise generator that represents the ripple added to $V_{\mathrm{BIAS}}$ by the bias generator and $Z_{\mathrm{IN}}$ is the impedance of the receiving LNA. The impedance $Z_{\mathrm{IN}}$ can model both the high input impedance of a voltage amplifier and the low input impedance of a charge amplifier or transimpedance amplifier. In Fig. 4, we also report the possible parasitic components (in gray): $C_B$is the parasitic capacitor of the resistor $R_B$ and ESR is the equivalent series resistance of the decoupling capacitor $C_C$. We will use them to assess the influence of the parasitic components on the results of the present analysis (Section II-D).

In order to analyze the effect of the biasing circuit on the CMUT signal and on the bias generator ripple noise, we introduce a special version of signal-to-noise ratio, called signal-to-ripple ratio (SRR), relating it to both voltage and

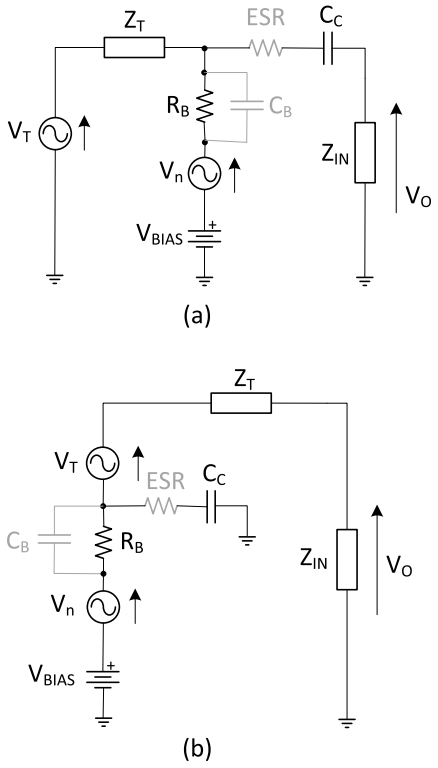


Fig. 4. Thévenin schemes of the CMUT with (a) direct biasing and (b) indirect biasing. Gray: the parasitic components.

current signals. The output SRR for the voltage signals is given by

$$\mathrm{SRR}_{\mathrm{OUT}}^{V} = \left|V_T^{\mathrm{OUT}}\right|^2 / \left|V_n^{\mathrm{OUT}}\right|^2 \tag{9}$$

and, for the current signals, by

$$\mathrm{SRR}_{\mathrm{OUT}}^{I} = \left|I_T^{\mathrm{OUT}}\right|^2 / \left|I_n^{\mathrm{OUT}}\right|^2. \tag{10}$$

Thus, it can be shown that for any value of $Z_{\mathrm{IN}}$, i.e., for any kind of receiving LNA, the two SRR values, (9) and (10), are the same

$$\mathrm{SRR}_{\mathrm{OUT}}^{V} = \mathrm{SRR}_{\mathrm{OUT}}^{I} = \mathrm{SRR}_{\mathrm{OUT}}. \tag{11}$$

Moreover, even if the CMUT "signal" and bias generator "ripple" sources are not located in the same part of the circuit, we define the "input" voltage SRR as

$$\mathrm{SRR}_{\mathrm{IN}} = |V_T|^2 / |V_n|^2 \tag{12}$$

with the aim of studying how these two signals are affected by the different biasing circuits.

### *A. Direct Biasing*

Following the definitions indicated above, we compute the output SRR of the *direct biasing* circuit in Fig. 4(a), which is:

$$\mathrm{SRR}_{\mathrm{OUT}} = \mathrm{SRR}_{\mathrm{IN}} \cdot \frac{R_B^2}{|Z_T|^2}. \tag{13}$$

Equation (13) shows that the output SRR linearly depends on the $R_B^2$ resistance and inversely on the square of the CMUT equivalent impedance $Z_T$. Since the CMUT impedance

$Z_T$ is fixed by the specific design, one can increase the bias resistor $R_B$ to improve the noise rejection of the circuit. In fact, the ripple signal is low-pass filtered by the bias resistor and the CMUT impedance. Therefore, $R_B$ may be chosen large enough to obtain a cutoff frequency below the operation band. However, the choice of the maximum $R_B$ value is limited by the parallel resistance of the CMUT, representing the dielectric loss, which causes a bias voltage division.

### B. Indirect Biasing

The output SRR of the *indirect biasing* circuit of Fig. 4(b) is given by

$$\mathrm{SRR_{OUT}} = \mathrm{SRR_{IN}} \cdot \left( \frac{R_B + |Z_C|}{|Z_C|} \right)^2 \tag{14}$$

where $|Z_C|$ is the impedance magnitude of $C_C$.

Equation (14) shows that, for the *indirect biasing* configuration, the output SRR directly depends on the squared sum of $R_B$ and $|Z_C|$ and inversely on the square of $|Z_C|$, while it is not dependent on the CMUT equivalent impedance $Z_T$. Thus, for a CMUT device in reception using an *indirect biasing* circuit, the SRR improves when the capacitance $C_C$ is very large, because it shunts to ground the ripple signal generated by the bias generator. The choice of $R_B$ must be performed similarly to the *direct biasing* case.

### C. Comparison Between the Two Biasing Circuits

To compare the two biasing circuits under investigation, we propose a figure of merit (FoM) named "ripple figure" (RF). We define the RF of a network as the ratio of the input SRR to the output SRR

$$\mathrm{RF} = 10 \cdot \log \left( \frac{\mathrm{SRR_{IN}}}{\mathrm{SRR_{OUT}}} \right)$$

and, for the proposed circuits in particular, we evaluate

$$\mathrm{RF_{direct}} = 20 \cdot \log \left( \frac{|Z_T|}{R_B} \right) \tag{15}$$

$$\mathrm{RF_{indirect}} = 20 \cdot \log \left( \frac{|Z_C|}{|R_B + Z_C|} \right) \tag{16}$$

which represent the decrease in the SRR introduced by the two networks, respectively. Unlike the classical "noise figure" (NF) [28], which is defined always positive (NF $\geq$ 0), the RF may assume negative values, indicating that noise, i.e., the bias generator ripple, is attenuated by the network (i.e., the biasing circuit).

As an example, we numerically evaluated the FoMs for the *direct* and *indirect biasing* circuits using the electrical characteristics $Z_T$ of a CMUT array element previously realized [15], [19], biased at 220 V, with $R_B = 1$ MΩ and $C_C = 100$ nF. The main parameters of the CMUT array element are reported in Table I.

Fig. 5 shows the RF values computed in the 1–30-MHz range. The *indirect biasing* circuit features an SRR improvement of about 70 dB, compared with the direct *biasing circuit*, making this configuration preferable, yet keeping in mind its safety-related aforementioned limitations.

TABLE I
CMUT PARAMETERS

| | |
|---|---|
| Cell plate diameter, μm | 29.6 |
| Cell Electrode diameter, μm | 20 |
| Cell-to-cell lateral distance, μm | 3.4 |
| Plate thickness, μm | 1.5 |
| Gap height, μm | 0.25 |
| Number of cells composing one array element | 637 |
| Array element electrical impedance[a], Ω | 167 - j 618 |
| Two-way center frequency (- 6dB), MHz | 10.8 |
| Fractional bandwidth (- 6dB), % | 104 |

[a] measured at 10 MHz using a bias voltage of 220 V

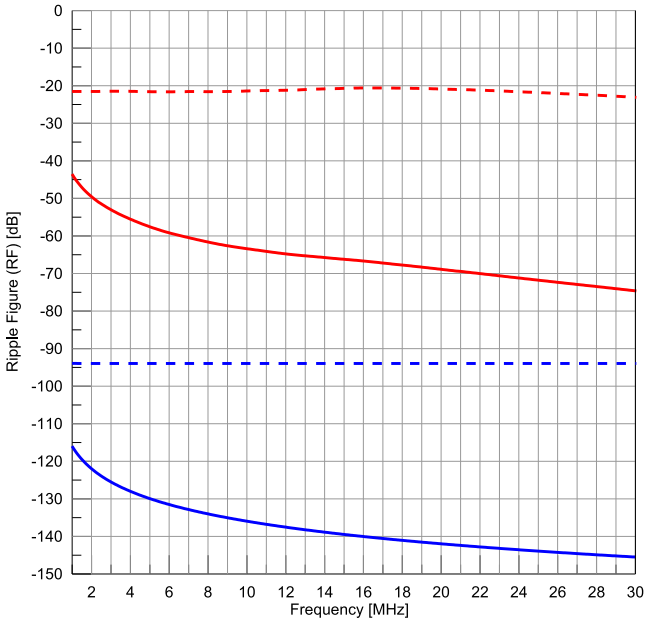


Fig. 5. RF of the direct biasing (red solid line) and indirect biasing (blue solid line) circuits. The dashed lines represent the same quantities, but considering the parasitic capacitance $C_B$ (2 pF in this example) in parallel to the bias resistance $R_B$.

### D. Influence of Parasitic Components

We also analyzed how the performance of the *direct* and *indirect* biasing circuits, in terms of ripple rejection, change by including the effects of the parasitic components (in gray in Fig. 4). In particular, we repeated the previous analysis by accounting for the ESR of the capacitance $C_C$ and the parasitic capacitance $C_B$ of resistor $R_B$.

In the *direct biasing* configuration, the parasitic capacitance $C_B$ can drastically affect the ripple-rejection characteristics of the circuit, whatever the value of $Z_{\mathrm{IN}}$. In fact, considering the values of the components mentioned in the previous section, and assuming a parasitic capacitance of 2 pF (including both the resistor package and the printed circuit board (PCB) pads and routes), we computed the output SRR value using in (13) the parallel $R_B$–$C_B$ instead of $R_B$. Fig. 5 depicts the corresponding RF value, using a red dashed line, showing that the ripple rejection is drastically lowered by this parasitic component, compared with the ideal case. On the other hand, the influence of the ESR of the decoupling capacitance $Cc$ is less important.

In the *indirect biasing* configuration, the dependence of the output SRR on $R_B$ and $Z_C$ is clearly shown in (14). In this

case, both the parasitic capacitance $C_B$ of the resistor $R_B$ and the ESR of the decoupling capacitance $Cc$ significantly affect the ripple-rejection capability of the circuit. In fact, the output ripple-noise contribution, due only to the parasitic capacitance of $R_B$ (i.e., considering an ideal $C_C$), may significantly increase the RF, regardless of the $Z_{\mathrm{IN}}$ value. In Fig. 5, the blue dashed line depicts the RF, computed by considering the same $C_C$, $C_B$, and $R_B$ values of the previous example. In a similar manner, in the case of an ideal $R_B$, the RF is worsened by the ripple-noise contribution due exclusively to the ESR. As an example, the computation of RF considering $C_B = 0$ F and ESR $= 10\ \Omega$ yields to equivalent results.

The combined effect of both parasitic components on the ripple-rejection capability may possibly almost nullify the margin that the *indirect biasing* circuit theoretically provides, compared with the *direct biasing* circuit. Therefore, a careful choice of the $C_C$ capacitor (with respect to the ESR and leakage resistance) and of the $R_B$ resistor package, and convenient design of the PCB layout (with the aim of minimizing the parasitic capacitance) are key aspects in CMUT bias-coupling circuit design.

## III. Proposed CMUT Biasing Generator Architectures

The reduction of the output voltage ripple in HV dc power supplies has been the subject of several papers presented in the literature, but not in circuits using CMUTs. More or less complex solutions have been proposed, among which the more sophisticated ones allow reducing the residual ripple in the order of $10^{-5}$ times the output voltage.

In this section, we introduce two different power-supply architectures that are well suited to be used as CMUT biasing generators. The first circuit proposed uses a quite conventional approach, where the topology was optimized for this specific use. The second circuit is based on an unconventional topology, using off-the-shelf components usually employed in other applications. The different peculiarities of two proposed circuits in terms of noise performance, power efficiency, and dimensions make them suitable for different applications.

The circuits are described in Sections III-A and III-B. Section III-C is dedicated to the analysis of their performance in actual operating conditions, i.e., in conjunction with a CMUT probe and an ultrasound scanner, with a focus on the dynamic behavior and on energetic aspects.

### A. High-Voltage Low-Noise Sinusoidal Biasing Circuit

The first circuit we propose uses a low-noise sinusoidal power oscillator. The system (Fig. 6) consists of an oscillator, which generates a 200-kHz sinusoidal carrier, and a tuned amplifier, whose output is fed to the input of a power amplifier. The output of the power amplifier is in turn connected to a full-wave rectifier, followed by a chain of notch filters (tuned at 200 kHz) to attenuate any possible residual high-frequency contributions generated by the oscillator on the dc output.

Here, we provide a more detailed description of each component of this architecture. The oscillator stage is a classical Hartley sine-wave oscillator, tuned at ~200 kHz. This type of oscillator has the following advantages.

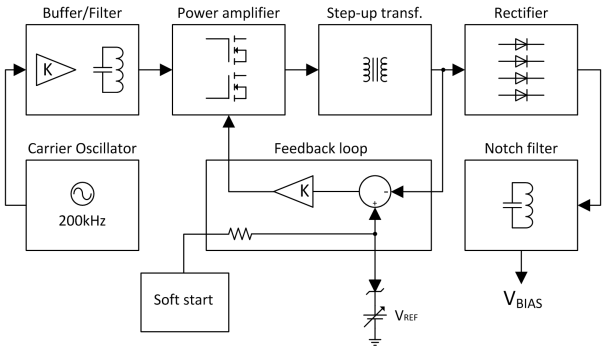


Fig. 6. Block diagram of the low-noise HV sinusoidal power supply circuit.

1) It has a good stability.
2) It requires few components, and thus it is simple to realize.
3) It also produces a good-quality sine wave, since the amplifier is connected in a common drain configuration (which guarantees a low output impedance) and has a local feedback factor equal to 100% (which improves the linearity of the circuit).

The signal generated by the oscillator is then sent to a buffer amplifier, before reaching the power section (Fig. 6).

From an energy point of view, the power supplied by the oscillator is sufficient to drive the power amplifier, which is built around a pair of MOSFET devices that require an extremely low power level to be driven. Thus, the power amplifier can be directly connected to the oscillator stage. Anyway, the buffer was added in this topology in order to maintain a high stability of the oscillator frequency, so as to avoid excessive frequency drift, which would bring the tuned cells of the output *LC* filters out of resonance. Actually, the oscillator resonance frequency is relatively sensitive to variations of the external load indeed, particularly when the load is represented by a power amplifier.

The amplifier output is connected to the elevation transformer, which has a turns ratio of 60:1, and then to the full-wave rectifier to convert the sine wave into a dc voltage.

The dc signal at 400 V is then sent to a group of four *LC* cells, which make up a notch filter tuned at ~200 kHz, as mentioned before. This circuit is designed to have also a low-pass filter characteristic, so as to attenuate the higher frequency harmonics introduced by the full-wave rectifier.

Finally, the HV generator is equipped with a feedback circuit that stabilizes the output signal to the value set by the reference voltage (Fig. 6). Moreover, a soft-start system makes the output voltage vary linearly at a rate of 40 V/s, starting from zero up to the maximum set value. This soft-start function is used to avoid a too rapid growth of the bias voltage of the CMUT when the device is turned ON.

The ripple signal resulting from this type of circuit exhibits a low level at the oscillation frequency (which is far below the CMUT operation band), and it is substantially free from higher order harmonics. These characteristics make it suitable to be conveniently used with the bias coupling circuits previously analyzed, without the need to minimize the parasitic effects of the used components.

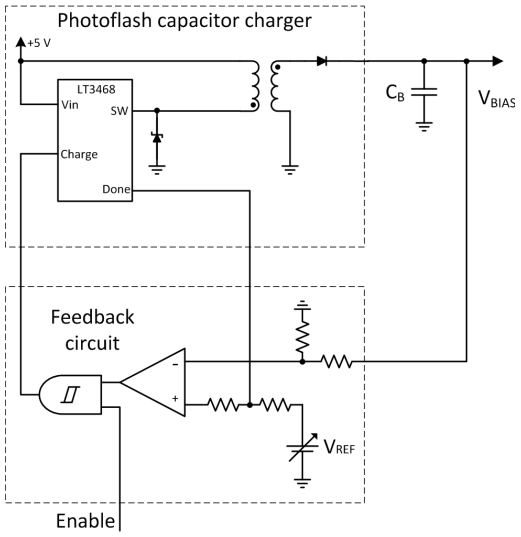


Fig. 7. Low-noise HV synchronous power supply circuit, with the external trigger signal.

### *B. High-Voltage Synchronous Biasing Circuit*

The second circuit we propose (Fig. 7) exploits the CMUT peculiarity of behaving as a practically ideal capacitor under dc conditions. Therefore, once charged, a CMUT does not absorb dc current from the bias voltage generator, except for a typically negligible dielectric leakage current.

The basic idea of this biasing circuit is to turn OFF the circuit that generates the HV during the reception cycle of the CMUT. The device is fed only by the charge stored in a "buffer capacitor" ($C_B$ in Fig. 7), which is recharged in a specific time interval determined by the ultrasound scanner connected to the CMUT probe [8], [29]. The noise ripple related to the charge of the buffer capacitor $C_B$ is thus confined to short intervals, during which the scanner is not performing signal acquisition. This solution allows obtaining a bias voltage free from residual superimposed ripple, which minimizes the overall noise of the system.

The active element in the high-voltage synchronous biasing (HV-SB) circuit is represented by an IC implementing a photoflash capacitor charger (LT3468, Linear Technology Corporation, Milpitas, CA, USA), which uses a flyback transformer to charge the capacitor up to 300 V by sensing the characteristics of the flyback pulse.

In order to be able to control the HV bias voltage level below 300 V, we introduced a feedback circuit that compares the output voltage with a reference voltage and produces a feedback logic signal, which is fed to the *Charge* control input to conveniently truncate the charging cycle. Such a feedback circuit uses a low-power comparator and an AND logic port. These two components are both powered by the *Enable* logic signal coming from the ultrasound scanner, which is set "high" to enable the charging of the buffer capacitance. Therefore, the feedback circuit is also turned OFF during the time in which the CMUT device is active, in order to minimize any possible noise contribution on the dc bias.

More in detail, the feedback circuit implements the following logical operation. If the *Enable* signal is "low," the *Charge* input of the photoflash capacitor charger is disabled, and the circuit absorbs only a quiescent current of 1 $\mu$A. If the *Enable* signal is "high," the *Charge* input is set only when the output bias voltage, conveniently scaled by a voltage divider, becomes lower than the reference voltage ($V_{\mathrm{REF}}$).

This simple circuit permits to accurately adjust the voltage in a range of 0–300 V, with a response time compatible with typical ultrasound scan timing. The circuit dimension is about 1.5 cm$^2$, making it suitable to be housed into a medical imaging probe case.

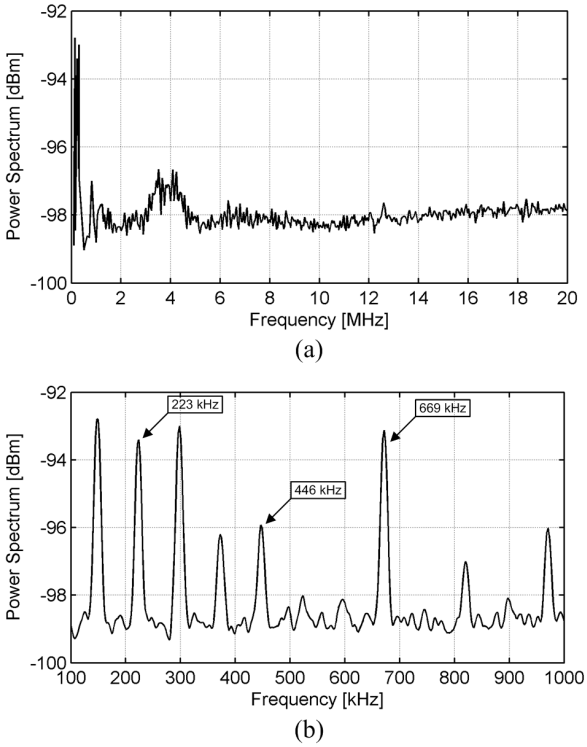


Fig. 8. Power spectrum of the output noise of the (a) HV-LNSB circuit plotted in the 1–20 MHz frequency range and (b) its magnified view in the 100 kHz–1 MHz range. The effective frequency oscillation of the sinusoidal generator is 223 kHz. The other peaks shown in (b) are due to the external power supply used to supply the circuit under test.

### *C. In-System Performance*

We now analyze the two circuits in a typical application context, i.e., in conjunction with an ultrasound scanner. The purpose of the bias voltage generator is to supply the CMUT with a bias voltage, while providing enough power to restore the static charge variation due to two phenomena. The first phenomenon is the dielectric leakage current of the capacitors. The second phenomenon is related to the nonideal shape of the bipolar excitation pulses, often characterized by unsymmetric positive and negative half-cycles, which may introduce a dc component, causing a variation of the CMUT bias voltage. The extent of these two phenomena determines the current requirement.

Without loss of generality, let us consider the case of a 1-D CMUT array probe biased through a *direct biasing* circuit.

In the case of the high-voltage low-noise sinusoidal biasing (HV-LNSB) configuration, the leakage current related only to a CMUT 1-D array element, which is typically in the nanoampere range, allows adopting bias resistance values in

the megaohm range, resulting in a total power request in the order of tens of microwatts.

In the case of the HV-SB configuration, the total leakage current is dominated by the one related to the buffer capacitor, which is in the microampère range, resulting in a total average power request in the order of hundredths of microwatts. For this particular circuit configuration, in which the buffer capacitor charge is restored in defined "dead" time intervals, the current request influences the dynamic operation of the ultrasound scanner, i.e., the image frame rate.

In both circuit configurations, the bias voltage level, after a bipolar pulse is applied by the ultrasound scanner to excite the CMUT, may be different from the one supplied by the generator. The voltage difference causes a charge variation, resulting in a further current requirement that may be determined as follows.

Let us suppose that the voltage across the CMUT electrodes, after an excitation pulse, is $V_C(0) \neq V_{\text{BIAS}}$, at $t = 0$ s. The bias voltage generator output current, flowing through the bias resistor $R_B$ to restore the CMUT charge, is given by

$$i(t) = -\left(\frac{\Delta V}{R_B}\right) \cdot e^{-\frac{t}{\tau}} \tag{17}$$

with $\Delta V = V_C(0) \pm V_{\text{BIAS}}$, whereas the voltage across the CMUT is given by

$$V_C(t) = \Delta V \cdot e^{-\frac{t}{\tau}} + V_{\text{BIAS}}. \tag{18}$$

In (17) and (18), $\tau = R_B \cdot C_{\text{CMUT}}$ and $\tau = R_B \cdot ((C_B \cdot C_{\text{CMUT}})/(C_B + C_{\text{CMUT}}))$ represent the time constant for the HV-LNSB and the HV-SB topology, respectively. The energy supplied by the bias voltage generator, after each excitation pulse, is

$$U_g(t) = (\Delta V)^2 \cdot C_{\text{CMUT}} \cdot (1 - e^{-\frac{t}{\tau}}) \tag{19}$$

with $0 \text{ s} < t < T_p$, being $T_p$ the pulse repetition time. If $\tau < T_p$, the average power supplied by the bias voltage generator is

$$W_g \cong \frac{(\Delta V)^2 \cdot C_{\text{CMUT}}}{T_p}. \tag{20}$$

Therefore, in order to avoid any drift of the bias voltage due to an unideal excitation pulse shape, the time constant $\tau$ should be reduced by choosing $R_B$ and $C_B$, respectively, small and large enough, in order to match the maximum pulse repetition rate required by the application. However, the resistor $R_B$ cannot be too small, as its value influences both the ripple rejection capability of the bias voltage coupling circuit and the reception frequency response of the CMUT.

As an example, we compute the time constant and the average power demand in a linear-scan imaging scenario. By considering a 1-D CMUT array featuring an element capacitance of 20 pF, biased through a 1-MΩ resistance, we evaluate the equivalent electrical load on the bias voltage generator when 64-element subapertures are simultaneously excited and linearly scanned, resulting in a total capacitance of about $C_{\text{CMUT}} \cong 1.3$ nF and a biasing resistance of $R_B \cong 15$ kΩ. If each excitation pulse causes a bias voltage variation of, e.g., 5 V, the time constant is $\tau = 19.5$ $\mu$s.

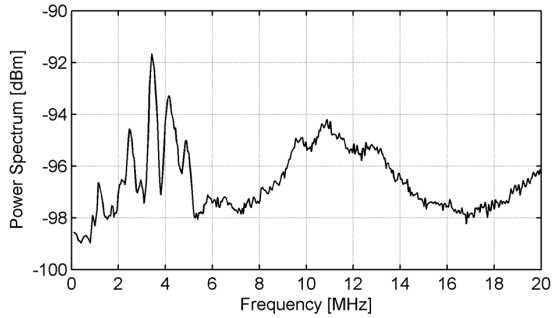


Fig. 9. Power spectrum of the HV-SB circuit when disabled.

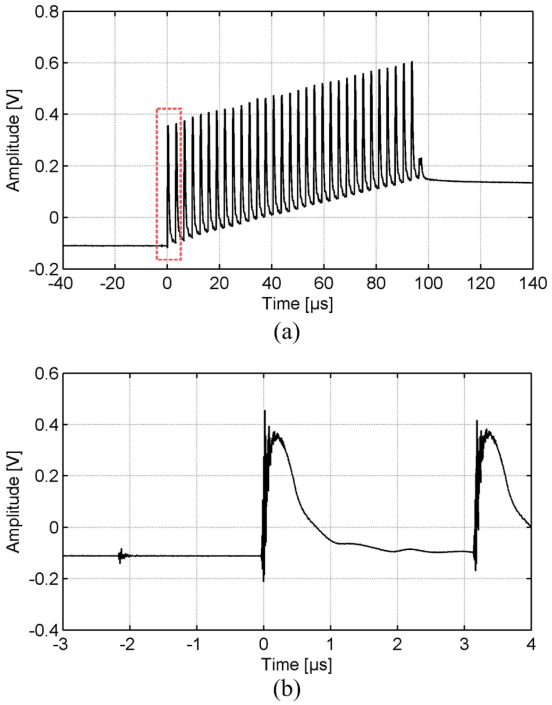


Fig. 10. Time-domain measurement of the HV-SB circuit during the "turn-ON" period. The dashed area in (a) is shown in (b).

Considering a pulse repetition period of about 10 times the time constant, i.e., 200 $\mu$s, the average power is approximately 0.16 mW.

## IV. Characterization

This section is dedicated to the characterization of two bias generator prototypes based on the proposed architectures previously described and analyzed. Two different techniques were used to measure the output residual ripple. B-mode imaging experiments were also carried out to test the dynamic behavior of the circuits in a real ultrasound imaging experimental setup.

### *A. High-Voltage Low-Noise Sinusoidal Biasing Circuit*

To characterize the HV-LNSB circuit, we carried out power-spectrum measurements. These provide the most suitable approach to analyze and quantify the output ripple level and frequency spectrum.

The measurement was made using an HP3588A spectrum analyzer (Hewlett–Packard, Inc., Palo Alto, CA, USA). The measurement scheme in the frequency domain uses a 50-Ω

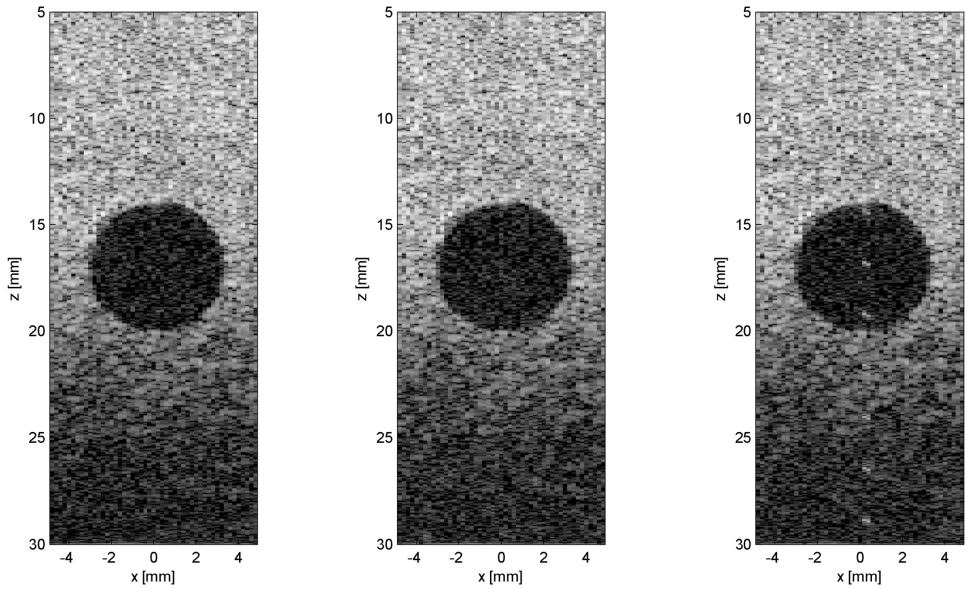


Fig. 11. B-mode images of a tissue-mimicking phantom obtained with a CMUT probe biased at 220 V using (a) direct biasing circuits and HV-LNSB, (b) synchronized HV-SB, and (c) not-synchronized HV-SB generators.

coaxial cable across the HV-LNSB output, which goes through a dc blocking capacitor and ends with a 50-Ω termination at the input of the spectrum analyzer. The dc blocking capacitor prevents any dc current from passing through to the spectrum analyzer; it also avoids dc loading effects.

The measurement results are shown in Fig. 8. The peak due to the local sinusoidal oscillator has a frequency of 223 kHz. The second harmonic (446 kHz) level is −3 dB, while the third harmonic has approximately the same value of the first, due to the inaccurate centering of the notch-filter stage. However, the level of the residual ripple is quite low, i.e., it is less than 5 $\mu$V on the 50-Ω load up to 1 MHz and lower than 6 $\mu$V up to 20 MHz. The measured ripple levels obtained with the proposed HV-LNSB circuit match the initially mentioned requirements.

### *B. High-Voltage Synchronous Biasing Circuit*

As stated before, during pulse-echo operation, the ultrasound scanner disables the HV-SB circuit that generates the high biasing voltage. During this time interval, the CMUT is biased by the voltage held by the "buffer capacitor" $C_B$. When the bias voltage becomes lower than a specific threshold voltage ($V_{\mathrm{REF}}$), $C_B$ is recharged in a time interval determined by the ultrasound scanner. In these conditions, we achieve a bias voltage free from residual ripple, which minimizes the overall noise of the system.

First, we performed power spectrum measurements using the same method as in Section IV-A. The output of the HV-SB circuit was connected to the input of the spectrum analyzer using a 100-nF decoupling capacitor. The voltage reference was set to achieve an output voltage of 220 V dc; the circuit was then enabled and successively disabled. Fig. 9 reports the power spectrum measured immediately after disabling the circuit, which shows an overall residual ripple level lower than 2.8 $\mu$V, likely attributable to external sources of noise.

The same frequency-domain measurement approach was not applicable to the HV-SB circuit during other operation modalities, due to the difficulties involved in the synchronization of the circuit itself with the power spectrum analyzer. Therefore, we carried out time-domain measurements using a TDS5034B oscilloscope (Tektronix, Beaverton, USA).

The output of the HV-SB circuit was connected to the input of the oscilloscope using a 100-nF decoupling capacitor. The circuit was then enabled with a constant signal. Fig. 10 shows the acquired voltage signal after the output voltage was settled to 220 V. Fig. 10(a) shows that, during the charging cycle of the buffer capacitance by means of the high-current (1.4 A) pulses generated by the photoflash IC, the ac component of the output voltage consists in a limited duration (100 $\mu$s) pulse train. The difference between the final and initial starting voltage values, which provide a measure of the sensitivity of the feedback circuit, is about 0.2 V (0.1% of the output dc voltage). Fig. 10(b) shows the first part of the pulse train, highlighting both the response time of the circuit, which is measured as the time interval between the first glitch (corresponding to the *Charge* trigger) and the first charging pulse, and the pulse shape of the charging pulses themselves. The response time is about 2 $\mu$s. Each pulse has a 0.5 V amplitude and a half-amplitude pulse length of less than 1 $\mu$s, while the pulse period is approximately 3 $\mu$s. The spectral content of such an ac voltage signal definitely falls in the ultrasound scanner operation band. In fact, if presented at the ultrasound front-end input during reception, this kind of signal generates a strong switching noise, visible in the reconstructed images. Moreover, the same signal acts unavoidably as an

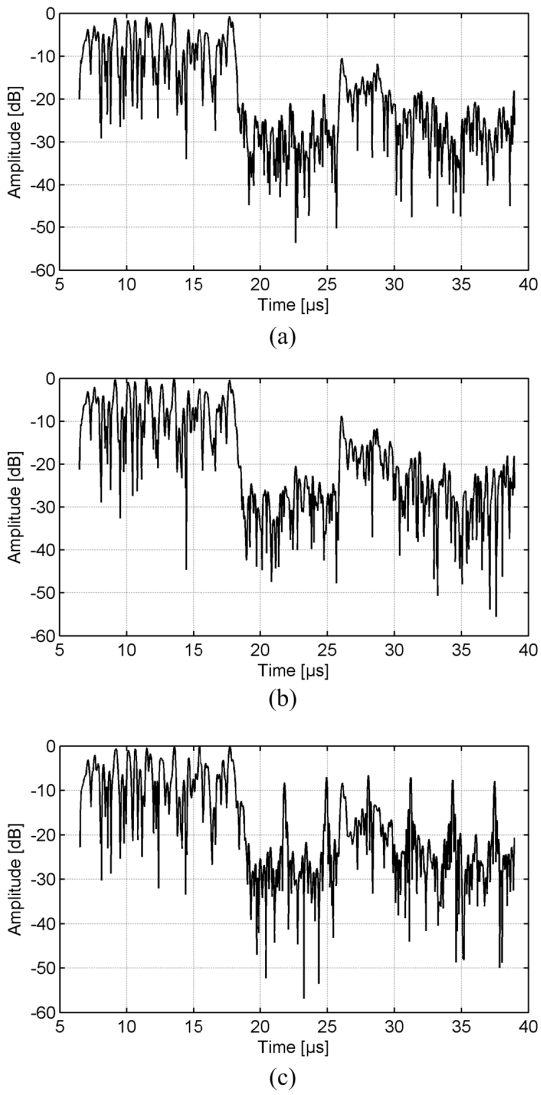


Fig. 12. Envelope of a scan line of the image corresponding to $x = 0.2$ mm obtained using the (a) HV-LNSB, (b) HV-SB, and (c) not-synchronized HV-SB generators.

excitation signal for the CMUT causing the transmission of a spurious acoustic pressure pulse.

The synchronization (*Enable*) signal, i.e., a periodic pulse wave, must be carefully designed by taking into account the current absorption of the CMUT probe, which determines the discharge rate of the buffer capacitor, and consequently the required charge quantity to be injected in order to restore the desired bias voltage. These characteristics determine the duration of the synchronization signal "high" level, which must be long enough to inject the desired charge, and the pulse wave period, which should be short enough to maintain the output voltage within the desired bias voltage accuracy. Furthermore, the synchronization signal must be conveniently timed with the ultrasound scanner beamforming sequence.

### C. Ultrasound Imaging Experiments

In order to practically test the operation and performance of the two circuits, we used a dedicated ultrasound imaging setup, which includes a 192-element linear CMUT active probe [15], a programmable ultrasound scanner (ULA-OP system, University of Florence, Florence, Italy [30]), and a CIRS tissue-mimicking ultrasound phantom (model 040GSE, CIRS, Inc., Norfolk, VA, USA). The 192 CMUT array elements were biased using *direct biasing* circuits located inside the probe. We scanned a portion of the phantom including a 5-mm-diameter anechoic cylinder embedded in a uniform background gel. The scanner software was programmed to perform linear scan beamforming using 32-element TX apertures, exciting the probe with two-cycle 10-MHz 40 V peak bursts. The TX focus was set to 18 mm. In RX, 64-element dynamically focused apertures were used. The RX beamformed signals were demodulated at 10 MHz and filtered with a 66% bandwidth. The pulse repetition frequency was set to 5000 Hz, allowing a depth of acquisition of 30 mm with a frame rate of 26 frames/s.

B-mode images were obtained using both the HV-LNSB and the HV-SB circuits to bias the CMUT probe at 220 V. We acquired a first image using the HV-LSNB. In the case of HV-SB, an external logic was used to generate the *Enable* signal of the bias generator and the pulse repetition signal of the ultrasound scanner. In this configuration, we acquired two images. The first image was achieved using an *Enable* signal with a 500-$\mu$s "high" level, activated 200 $\mu$s before each 192-line frame acquisition, which lasts 38.4 $\mu$s; the second image was achieved by holding the *Enable* signal "high" for the entire acquisition. Using these settings, we extracted one image frame for each case considered.

The three images are shown in Fig. 11. For the three images, we computed the average signal power obtaining equivalent values, proving that the CMUT was correctly biased with the expected 220 V voltage. In the case of the synchronized HV-SB [Fig. 11(b)], we evaluated the frame rate after the introduction of the charging cycle, resulting in 25.5 frames/s, i.e., 0.5 frames/s lower than the one achieved in normal operation scan conditions.

Finally, we show the impact of the HV-SB noise related to the charging cycle visible in Fig. 11(c). In Fig. 12, we show the envelope of an image scan line at $x = 0.2$ mm, using the HV-LNSB generator [Fig. 12(a)], the HV-SB generator [Fig. 12(b)], and the not-synchronized HV-SB generator [Fig. 12(c)]. While the first two lines are comparable, the third one shows that the noise signal is comparable or even greater compared with the beamformed echo signals.

## V. Conclusion

In this paper, we addressed the main set of problems related to HV biasing of CMUTs in ultrasound imaging applications. We recalled the two bias coupling circuits typically employed in CMUT-based imagers. We thoroughly analyzed their performance in terms of ripple rejection, proposing a basic set of rules for the choice of the single circuit components. The methods used in the analysis may assist the design of a CMUT-based imaging system by determining the noise requirements for the CMUT bias voltage generator. As a general guideline, the residual ripple level of the bias voltage generator should be lower than the input-referred root-mean-square noise level, taking into account the entire system

bandwidth, considering both the RF of the chosen biasing circuit and the maximum aperture size in terms of number of receiving array elements.

We proposed two bias voltage generator architectures, suitable to be used the first in classical ultrasound imaging systems and the second in ultramobile imaging applications. The latter, in particular, is based on a very small-area circuit that may be easily integrated inside the probe. This characteristic matches the actual trend of modern ultrasound imaging system development. Indeed, the effort of medical diagnostic system manufacturers is currently directed toward the development of small and portable devices, which can be interfaced with compact PCs or even tablets and smartphones, using standard low-cost cables or wireless connections [31]–[33].

Circuit prototypes, based on both proposed architectures, were fabricated and characterized in terms of ripple-noise performance. Finally, B-mode imaging experiments were carried out on an open ultrasound scanner using a previously developed CMUT linear probe biased with the two generator prototypes and *direct biasing* circuits. The dynamic behavior of the circuits was assessed by analyzing the generated ultrasound images, confirming the validity of the approaches and the related design methods.

## ACKNOWLEDGMENT

The authors would like to thank G. Rosi for collaborating on the development of the HV-LNSB sinusoidal power supply and Prof. M. Pappalardo for his precious reviews and comments. They would also like to thank the referees who have suggested substantial amendments to this paper that have enabled us to improve it in several aspects.

## REFERENCES

[1] R. Reeder and C. Petersen. *The AD9271-A Revolutionary Solution for Portable Ultrasound*. [Online]. Available: www.analog.com/en/analog-dialogue/articles/revolutionary-solution-for-portable-ultrasound.html

[2] M. Pappalardo, G. Caliano, A. Savoia, and A. Caronti, "Micromachined ultrasonic transducers," in *Piezoelectric and Acoustic Materials for Transducer Applications*, A. Safari and E. K. Akdogan, Eds. New York, NY, USA: Springer, 2008, pp. 453–478.

[3] M. I. Haller and B. T. Khuri-Yakub, "A surface micromachined electrostatic ultrasonic air transducer," in *Proc. IEEE Ultrason. Symp.*, Nov. 1994, pp. 1241–1244.

[4] X. Jin, I. Ladabaum, and B. T. Khuri-Yakub, "The microfabrication of capacitive ultrasonic transducers," *J. Microelectromech. Syst.*, vol. 7, no. 3, pp. 295–302, Sep. 1998.

[5] G. Caliano *et al.*, "Micromachined ultrasonic transducers using silicon nitride membrane fabricated in PECVD technology," in *Proc. IEEE Ultrason. Symp.*, vol. 1. Oct. 2000, pp. 963–968.

[6] O. Oralkan *et al.*, "Capacitive micromachined ultrasonic transducers: Next generation arrays for acoustic imaging?" *IEEE Trans. Ultrason., Ferroelect., Freq. Control*, vol. 49, no. 11, pp. 1596–1610, Nov. 2002.

[7] G. Caliano *et al.*, "Design, fabrication and characterization of a capacitive micromachined ultrasonic probe for medical imaging," *IEEE Trans. Ultrason., Ferroelect., Freq. Control*, vol. 52, no. 12, pp. 2259–2269, Dec. 2005.

[8] J. Williams, "High-voltage, low-noise, DC-DC converters," Linear Technol. Corp., Milpitas, CA, USA, Appl. Note 118, Mar. 2008. [Online]. Available: www.linear.com/docs/26421

[9] P. C. Eccardt, K. Niederer, T. Scheiter, and C. Hierold, "Surface micromachined ultrasound transducers in CMOS technology," in *Proc. IEEE Ultrason. Symp.*, vol. 2. Nov. 1996, pp. 959–962.

[10] A. S. Savoia *et al.*, "An ultra-low-power fully integrated ultrasound imaging CMUT transceiver featuring a high-voltage unipolar pulser and a low-noise charge amplifier," in *Proc. IEEE Ultrason. Symp.*, Sep. 2014, pp. 2568–2571.

[11] A. Bhuyan *et al.*, "Integrated circuits for volumetric ultrasound imaging with 2-D CMUT arrays," *IEEE Trans. Biomed. Circuits Syst.*, vol. 7, no. 6, pp. 796–804, Dec. 2013.

[12] M. Sautto *et al.*, "A CMUT transceiver front-end with 100-V TX driver and 1-mW low-noise capacitive feedback RX amplifier in BCD-SOI technology," in *Proc. 40th Eur. Solid State Circuits Conf. (ESSCIRC)*, Sep. 2014, pp. 407–410.

[13] P. Behnamfar, R. Molavi, and S. Mirabbasi, "Transceiver design for CMUT-Based super-resolution ultrasound imaging," *IEEE Trans. Biomed. Circuits Syst.*, vol. 10, no. 2, pp. 383–393, Apr. 2016.

[14] G. Gurun, P. Hasler, and F. L. Degertekin, "Front-end receiver electronics for high-frequency monolithic CMUT-on-CMOS imaging arrays," *IEEE Trans. Ultrason., Ferroelect., Freq. Control*, vol. 58, no. 8, pp. 1658–1668, Aug. 2011.

[15] A. S. Savoia, G. Caliano, and M. Pappalardo, "A CMUT probe for medical ultrasonography: From microfabrication to system integration," *IEEE Trans. Ultrason., Ferroelect., Freq. Control*, vol. 59, no. 6, pp. 1127–1138, Jun. 2012.

[16] A. Bagolini *et al.*, "PECVD low stress silicon nitride analysis and optimization for the fabrication of CMUT devices," *J. Micromech. Microeng.*, vol. 25, no. 1, p. 015012, Jan. 2015.

[17] A. Iula, A. S. Savoia, and G. Caliano, "Capacitive micro-fabricated ultrasonic transducers for biometric applications," *Microelectron. Eng.*, vol. 88, no. 8, pp. 2278–2280, Aug. 2011.

[18] A. Savoia *et al.*, "Design and fabrication of a CMUT probe for ultrasound imaging of fingerprints," in *Proc. IEEE Ultrason. Symp.*, Oct. 2010, pp. 1877–1880.

[19] A. S. Savoia, G. Caliano, B. Mauti, and M. Pappalardo, "Performance optimization of a high frequency CMUT probe for medical imaging," in *Proc. IEEE Ultrason. Symp.*, Oct. 2011, pp. 600–603.

[20] A. S. Ergun, G. Yaralioglu, and B. T. Khuri-Yakub, "Capacitive micromachined ultrasonic transducers: Theory and technology," *J. Aerosp. Eng.*, vol. 16, no. 2, pp. 76–84, Apr. 2003.

[21] S. Frew, H. Najar, and E. Cretu, "VHDL-AMS behavioural modelling of a CMUT element," in *Proc. IEEE Behavioral Modeling Simulation Workshop (BMAS)*, Sep. 2009, pp. 19–24.

[22] J. Zahorian, M. Hochman, S. Satir, and F. L. Degertekin, "Bias optimization of dual ring CMUT arrays for forward looking IVUS applications," in *Proc. IEEE Ultrason. Symp.*, Oct. 2010, pp. 447–450.

[23] F.-S. Lee and S.-C. Tseng, "Analysis of bias effects for a capacitive-micro-ultrasonic-transducer," in *Proc. IEEE/SICE Int. Symp. Syst. Integr. (SII)*, Dec. 2011, pp. 452–457.

[24] H. Koymen, A. Atalar, and H. K. Oğuz, "Designing circular CMUT cells using CMUT biasing chart," in *Proc. IEEE Ultrason. Symp.*, Oct. 2012, pp. 975–978.

[25] P. Behnamfar and S. Mirabbasi, "A CMUT read-out circuit with improved receive sensitivity using an adaptive biasing technique," in *Proc. IEEE Biomed. Circuits Syst. Conf. (BioCAS)*, Nov. 2011, pp. 397–400.

[26] G. Matrone, A. S. Savoia, G. Caliano, M. Terenzi, F. Quaglia, and G. Magenes, "A volumetric CMUT-based ultrasound imaging system simulator with integrated reception and $\mu$-beamforming electronics models," *IEEE Trans. Ultrason., Ferroelectr., Freq. Control*, vol. 61, no. 5, pp. 792–804, May 2014.

[27] A. Caronti, G. Caliano, A. Savoia, R. Carotenuto, and M. Pappalardo, "A low-noise, wideband electronic system for pulse-echo ultrasound imaging with CMUT arrays," in *Proc. IEEE Ultrason. Symp.*, Aug. 2004, pp. 2219–2222.

[28] H. T. Friis, "Noise figures of radio receivers," *Proc. IRE*, vol. 32, no. 7, pp. 419–422, Jul. 1944.

[29] A. Wu, "Photoflash capacitor chargers fit into tight spots," *Linear Technol.*, vol. 13, no. 4, pp. 2–6, Dec. 2003.

[30] P. Tortoli, L. Bassi, E. Boni, A. Dallai, F. Guidi, and S. Ricci, "ULA-OP: An advanced open platform for ultrasound research," *IEEE Trans. Ultrason., Ferroelect., Freq. Control*, vol. 56, no. 10, pp. 2207–2216, Oct. 2009.

[31] C. Antoine, E. Tarvin, S. Bharatan, U. Shah, R. O'Reilly, and M. Judy, "Reliability measurements of CMUT arrays of a semiconductor manufacturer," in *IEEE Int. Ultrason. Symp.*, Taipei, Taiwan, Oct. 2015.

[32] J. H. Kim, K. Park, I. Song, and Y. Yoo, "A real-time realization of the automatic b-mode image optimization on a smart mobile device for point-of-care ultrasound imaging," in *IEEE Int. Ultrason. Symp.*, Taipei, Taiwan, Oct. 2015.

[33] S. Ahn *et al.*, "Smartphone-based portable ultrasound imaging system: Prototype implementation and evaluation," in *Proc. IEEE Ultrason. Symp.*, Oct. 2015, pp. 1–4.

**Giosuè Caliano** (M'00–SM'13) received the M.S. degree in electronic engineering from the University of Salerno, Salerno, Italy, in 1993.

He was a Post-Graduate Fellow with the Department of Electronics, University of Salerno, both in didactic and research fields. In 1995, he joined Pirelli-FOS (SA, Italy) as an Industrial Automation Engineer and as a Design Engineer for optical fiber production. Since 1997, he has been the Head of the Acoustoelectronics Laboratory at the Department of Engineering, Roma Tre University, Rome, Italy. He is involved in design and characterization of micromachining ultrasonic transducers (CMUTs). In 2003, he obtained the first echographic images using a CMUT probe in conjunction with a commercial echographic system. Since 2012, he has been an Adjunct Professor of "Sensors and Transducers." In 2014, he obtained the "National Academic Qualification" as an Associate Professor of Electronics. He developed many types of CMUT transducers, from mono-element transducers to a 192-element probe for echographic imaging system. He has authored more than 110 papers on these fields published in international magazines and conference proceedings, and holds 11 international patents. He patented the new technology for CMUT fabrication called Reverse Process Technology. His current research interests include developing piezoelectric pressure sensors and measurement techniques for ceramics' characteristics.

Mr. Caliano was the Local Chair of the 2009 IEEE International Ultrasonics Symposium, held in Rome. He was the Founder of the International Workshop on CMUTs and has organized the event in 2001 at Rome, in 2011 at Salerno, and in 2016 at Rome.

**Giulia Matrone** (M'09) was born in Pavia, Italy, in 1985. She received the B.Sc. and M.Sc. degrees in biomedical engineering, both *cum laude,* and the Ph.D. degree in bioengineering and bioinformatics from the University of Pavia, Pavia, Italy, in 2006, 2008, and 2012, respectively.

She is currently a Research Fellow with the Bioengineering Laboratory, Department of Electrical, Computer, and Biomedical Engineering, University of Pavia. Her research interests are mainly in the field of ultrasound medical imaging; they include, ultrasound beamforming and imaging techniques, simulations, and system-level analyses for the design of 3-D ultrasound imaging probes.

**Alessandro Stuart Savoia** (M'03) was born in Edinburgh, U.K., in 1978. He received the Laurea and Ph.D. degrees in electronic engineering from Roma Tre University, Rome, Italy, in 2003 and 2007, respectively.

He holds a post-doctoral research position with the Department of Electronics Engineering, Roma Tre University, since 2007. From 2008 to 2010, he was a Co-Founder and Research and Development Manager, with an academic spinoff company of Roma Tre University in collaboration with the medical device company Esaote S.p.A., granted by the Italian Ministry of Education, for the industrial exploitation of the scientific results on MEMS-based ultrasonic transducers, most of them achieved during his Ph.D. and Post-Doctoral Research. In 2014, he became an Assistant Professor of Electronics with the Department of Engineering, Roma Tre University, where he has conducted research activity with the Acoustoelectronics Laboratory mainly in the field of ultrasonic transducers and their applications. During his scientific career, he was involved in analytical and FEM modeling, design, microfabrication and packaging, characterization, and electronics and system integration of MEMS-based capacitive micromachined ultrasonic transducers. He has authored or coauthored about 50 papers in international journals and conferences, and two book chapters. He holds four international patents. He has carried out consultancy activities as a Scientific Advisor in the field of acoustoelectronics for several semiconductor and medical device companies. His current research interests include piezoelectric ultrasonic transducers, and ultrasound beamforming and imaging techniques for medical and biometric application.